Science Advances
AAAS

advances.sciencemag.org/cgi/content/full/5/11/eaax2937/DC1

Supplementary Materials for

Exciton control in a room temperature bulk semiconductor with coherent strain pulses

Edoardo Baldini*, Adriel Dominguez, Tania Palmieri, Oliviero Cannelli, Angel Rubio, Pascal Ruello, Majed Chergui*

*Corresponding author. Email: ebaldini@mit.edu (E.B.); majed.chergui@epfl.ch (M.C.)

Published 29 November 2019, *Sci. Adv.* **5**, eaax2937 (2019)
DOI: 10.1126/sciadv.aax2937

This PDF file includes:

Supplementary Text

Section S1. Global fit analysis

To describe the significant parameters of the ΔR/R response, we performed a global fit analysis, by selecting nine temporal traces at different photon energies. Since our experimental data were measured up to 1 ns, our global fit analysis covered this long temporal window. The temporal signal comprises two contributions: i) the incoherent response caused by electron-hole cooling and recombination; and ii) The strongly damped sinusoidal modulation caused by the propagation of coherent acoustic phonons. These two contributions display very different weights across the probed spectral range: The incoherent signal is peaked around the c-axis exciton feature at 4.26 eV, whereas the coherent signal shows its maximum amplitude around 4.11 eV and decreases its weight with increasing probe photon energy. A satisfactory fit could be obtained by using two exponential functions (with relaxation time 42 ps and 270 ps) and a damped sinusoidal term convolved with a Gaussian response accounting for the temporal shape of the pump pulse.

Section S2. Generation mechanism

To quantify the electronic contribution to the photoinduced stress (σ_{DP}), we rely on the following expression

$$\sigma_{DP} = \sum_k \delta N(k) \frac{dE_k}{d\eta} \qquad \text{Eq. S1}$$

where δN(k) is the change of the electronic concentration at level k and $dE_k/d\eta$ is the deformation potential parameter. Given that after 50 fs (i.e. a much faster timescale than the detected coherent acoustic phonon period) the carriers have cooled to the bottom of the respective bands at Γ and ~ X (*16*), the expression can be simplified as

$$\sigma_{DP} = -NB\left[\left.\frac{dE_e}{dP}\right|_{\Gamma} + \left.\frac{dE_h}{dP}\right|_{X}\right] = -NB(d_e + d_h) \qquad \text{Eq. S2}$$

where N is the photoinduced carrier concentration, B is the bulk modulus and d_e (d_h) is the electron (hole) deformation potential parameter.

However, due to the extremely fast intraband relaxation of less than 50 fs (*16*), the electronic pressure can compete with the phononic pressure for the coherent acoustic phonon generation process. The phononic contribution to the photoinduced stress (σ_{TE}) can be written as

$$\sigma_{TE} = -\alpha_V B \Delta T_L = -\alpha_V B N\, E_{exc}/C_L \qquad \text{Eq. S3}$$

where α_V is the volumetric thermal expansion coefficient. For a tetragonal crystal, $\alpha_V = 2\alpha_\perp + \alpha_\parallel$, where $\alpha_\perp$ and $\alpha_\parallel$ are the in-plane and the out-of-plane thermal expansion coefficients, respectively. ΔT_L is the lattice temperature, C_L is the lattice heat capacity per unit volume and E_{exc} is the excess energy with respect to the optical bandgap energy. The ratio σ_{DP}/σ_{TE} reads

$$\frac{\sigma_{DP}}{\sigma_{TE}} = \frac{C_L(d_e + d_h)}{\alpha_V E_{exc}} \qquad \text{Eq. S4}$$

Substituting the computed values of d_h and d_e yields $\sigma_{DP}/\sigma_{TE} = -27.47$. Thus, we conclude that the deformation potential mechanism provides the dominant contribution to the generation of the observed coherent acoustic phonons. Importantly, this result can be obtained only with a reliable estimate of the deformation potentials, as the one provided at the GW level. In contrast, when relying on the generalized-gradient approximation level of density-functional theory (*36*), the value $\sigma_{DP}/\sigma_{TE} = -4.2$ is found.

Section S3. Phenomenological description of the observed exciton renormalization

In this section, we describe the origin of the large modulation of the exciton peak energy and oscillator strength using simple phenomenological arguments.

The modulation of the exciton peak energy arises from the combination of a large photoinduced strain ($\eta_0 = 0.1$-0.2%) and a large deformation potential parameter. It can be shown that the exciton shift can be written as

$$\delta E = B(d_e + d_h)\eta_0 \sim 30 - 40\ meV \qquad \text{Eq. S5}$$

which is in very good agreement with the experimental observations. However, we remark that this simple calculation involves only one energy within the exciton band. A full calculation over the whole probed energy range is possible only through our many-body perturbation theory calculations (Fig. 3B). In contrast, the modulation of the exciton peak amplitude depends on the photoelastic coefficients, which in our work have been computed within the Bethe-Salpeter equation (BSE) formalism. These photoelastic coefficients reach values up to 100 (Fig. 3C), which are two orders of magnitude larger than those found in GaAs (*46*). A comparison can be provided only with a full calculation, but the relative orders of magnitude can be appreciated by simply estimating the strain-induced change in the refractive index at the exciton resonance. For that, one can simply estimate the phonon-induced change of the real part of the refractive index n

$$\delta n = \frac{dn}{d\eta}\delta\eta \sim 10\% \qquad \text{Eq. S6}$$

In our experiments, we have observed around 5% change in the reflectivity ($\delta R/R$), which is in the same scale. Also our BSE calculation confirms that the variation is of the order of 3.5%.

Section S4. Perturbative model for coherent acoustic phonons

To simulate the change in the sample reflectivity produced by the propagating acoustic strain (δR/R), we rely on the perturbative approach developed in Ref. (*46*). Specifically, we make use of an expression that describes the time-dependent spatial overlap integral of the longitudinal coherent acoustic phonon strain field along the [010] direction (η(z, t)) with the back scattered light probe electric field (*34*)

$$\frac{\delta R}{R} = 2\Re\left\{\frac{4ik_0\tilde{n}}{1-\widetilde{n^2}}\frac{d\tilde{n}}{d\eta}\int_0^\infty \eta(z,t)e^{2ik_0\tilde{n}z}\,dz\right\} \qquad \text{Eq. S7}$$

where Re denotes the real part, z = 0 defines the TiO_2 surface, k_0 is the probe light wave vector in vacuum and $\tilde{n} = n_1 + in_2$ is the complex refractive index. In this expression, the exciton-phonon coupling parameter is represented by the photoelastic coefficient $d\tilde{n}/d\eta$, which can be written as

$$\frac{d\tilde{n}}{d\eta} = \frac{dn_1}{d\eta} + i\frac{dn_2}{d\eta} = \frac{dE}{d\eta}\left(\frac{dn_1}{dE} + i\frac{dn_2}{dE}\right) \qquad \text{Eq. S8}$$

Here, the quantity dE/dη represents the deformation potential parameter and it is assumed to be independent of the probe photon energy and the strain itself. We first utilized the traditional approach of ultrafast acoustics by computing the above expression over the probed spectral range. Here, we assumed the pulse strain profile to have a bipolar shape, as the carrier diffusion is negligible during the timescale of the detected acoustic field and the time window over which the phenomena are observed is too short for the acoustic pulse to lead to N-wave or to soliton formation. The sound velocity v = 9100 m/s was taken from the literature (*47*), the deformation potential parameter is computed from ab initio calculations, and the terms dn_1/dE and dn_2/dE are generated from our experimental steady-state optical data (fig. S1A). The results, shown in fig. S1B, have a poor agreement with the measured temporal traces.

In order to account for acoustic nonlinearities, we employed a more advanced approach, which relied on the direct involvement of many-body perturbation theory calculations in the evaluation of the photoelastic coefficients $dn_1/d\eta$ and $dn_2/d\eta$ themselves (as described in detail in §S4). The results are shown in Fig. 3D of the main text, in which we compare the experimental traces with the simulated signal from the coherent acoustic phonon. Here, we only had to multiply by -1 the traces above 4.30 eV in order to match the experimental curves. This implies that our refined calculation does not reproduce the phase of the signal in a specific portion of the spectrum, which is due to an only partial agreement between the theoretical photoelastic coefficient and the experimental one. Figure S2 shows the computed acoustic response in an enlarged scale (dotted lines), together with its fit to a damped sinusoidal function (solid lines). The frequency extracted from the fit to the computed traces are shown in Fig. 2E of the main text.

Section S5. Additional many-body perturbation theory calculations

We solved the BSE on top of GW electronic structure calculations to compute the electrodynamic properties of pristine anatase TiO_2. Figure S3A,B shows the real and imaginary part of the dielectric function calculated in the case of the unstrained unit cell (blue curves), and in the presence of a 0.2% tensile (red curves) and compressive (green curves) strain along the [010] axis, respectively. The calculation was performed over the 1.50-5.50 eV energy range, but we display the data between 3.50 eV and 5.50 eV for clarity. The resulting photoelastic coefficients $dn_1/d\eta$ and $dn_2/d\eta$ for the cases of tensile (red curves) and compressive (green curves) strain are presented in fig. S4A,B, as computed with the method of backward and forward differences, respectively. We observe an asymmetry between the photoelastic coefficients, which suggests a departure from the assumption that the photoelastic coefficients are independent of the applied strain direction. This effect can be understood by considering a Taylor expansion to the complex refractive index $\tilde{n}$

$$\tilde{n} = \widetilde{n_0} + \frac{d\tilde{n}}{d\eta}\eta + \frac{1}{2}\frac{d^2\tilde{n}}{d\eta^2}\eta^2 \qquad \text{Eq. S9}$$

We note that if the strain η changes its sign (compression-expansion), then the existence of non-vanishing second-order term explains the asymmetric variation of the refractive index ($\Delta\tilde{n} = \tilde{n} - \tilde{n}_0$) for compression/expansion. We also verified that the solution of the BSE on top of GW electronic structure calculations is necessary to reproduce our experimental results. To this aim, we computed the optical properties of an equilibrium (unstrained) and of a strained anatase TiO_2 unit cell in the absence of excitonic correlations, i.e. at the random-phase approximation (RPA) level on top of the same GW electronic structure calculations. Figure S5A shows the ε_{1c}, ε_{2c} in the case of the unstrained and in presence of the strain along the [010] axis. Thereafter, we compared these results with those obtained at the BSE level of theory. Figure S5B shows that ε_{2c} in the RPA-GW scheme features a large energy gap, which does not find agreement with the experimental findings. These results are in accordance to the calculations reported in our previous study (*7*). Finally, in fig. S5C,D, we compare the photoelastic coefficients $dn_1/d\eta$ and $dn_2/d\eta$ within the two levels of theory, and observe that their shape and magnitude undergo a strong renormalization when excitonic effects are taken into account. Importantly, our experimental results can be reproduced just within the BSE-GW level of theory.

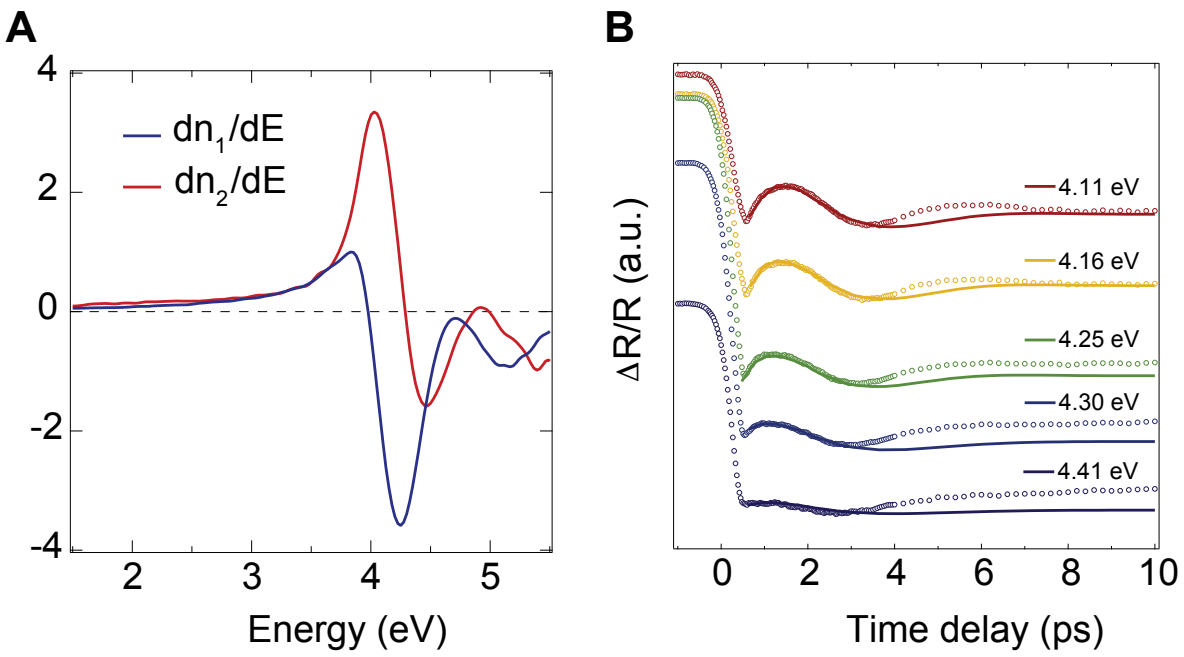

Fig. S1. Traditional approach of ultrafast acoustics applied to anatase TiO_2. (A) Energy derivatives of the real and imaginary parts of the refractive index, as obtained from our spectroscopic ellipsometry measurements at RT. (B) Transient acoustic response at different probe photon energies (solid lines), as simulated with the traditional approach of ultrafast acoustics (i.e. making use of the quantities reported in fig. S1A). The dotted lines are the experimental data.

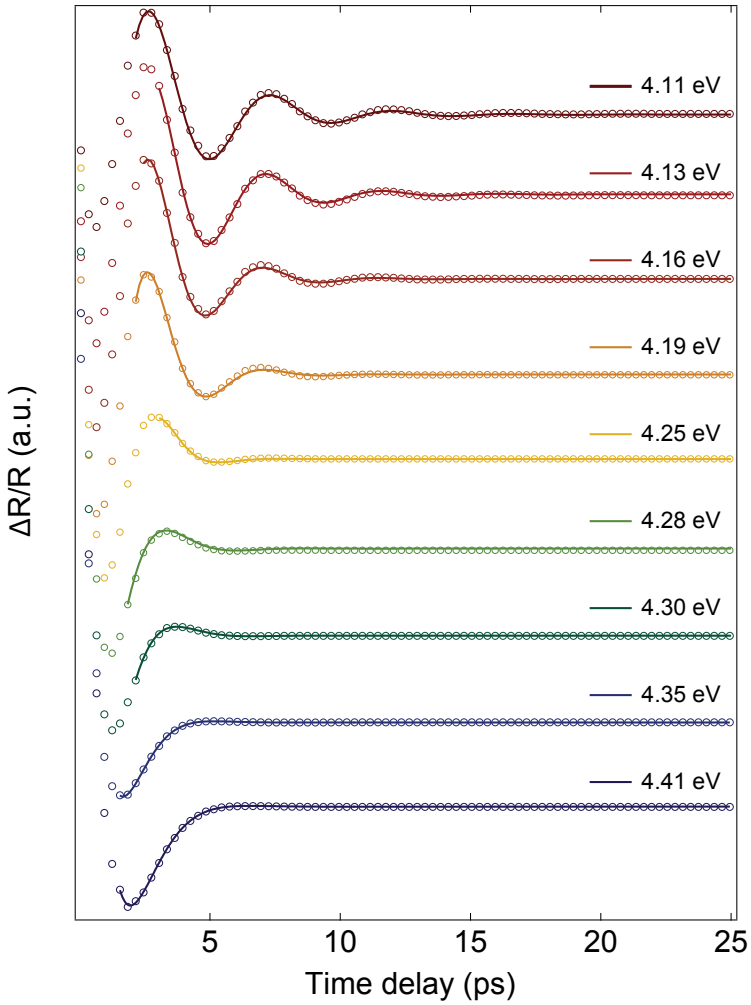

Fig. S2. Simulation of the transient acoustic signal. Computed acoustic response (dotted lines), together with its fit to a damped sinusoidal function (solid lines). The probe photon energies are indicated in the labels.

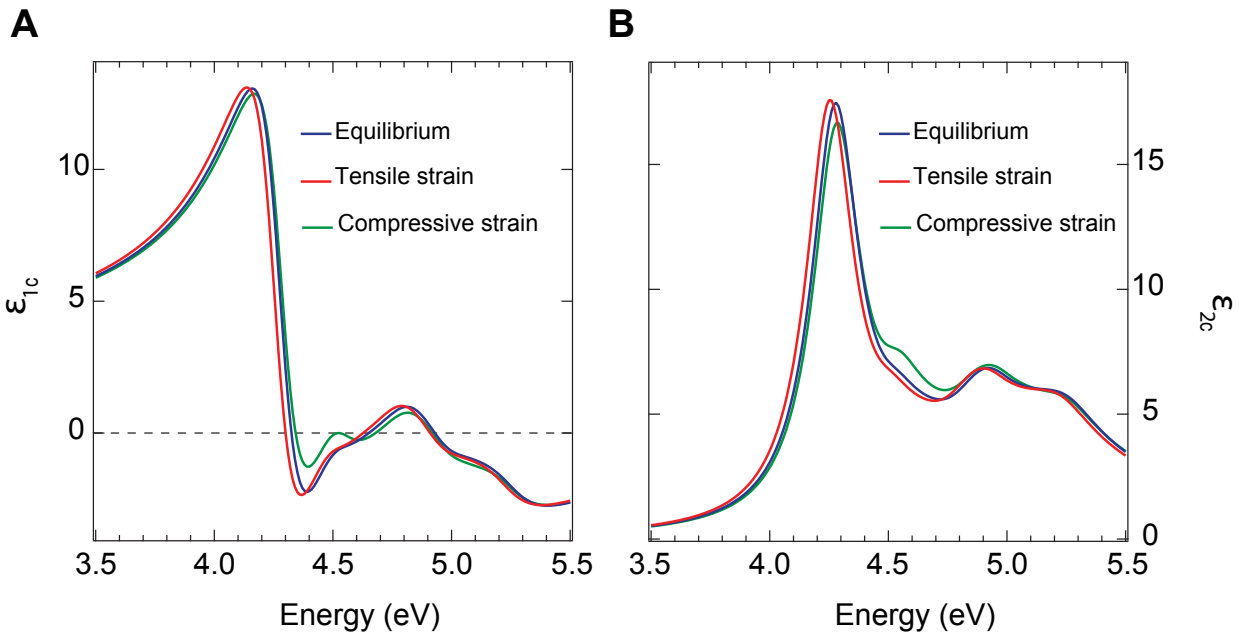

Fig. S3. Many-body perturbation theory calculations on the strained unit cell. Calculated (A) real and (B) imaginary part of the dielectric function in the BSE-GW scheme for the equilibrium unit cell (blue curve) and in the presence of a 0.2% tensile (red curve) and compressive (green curve) strain.

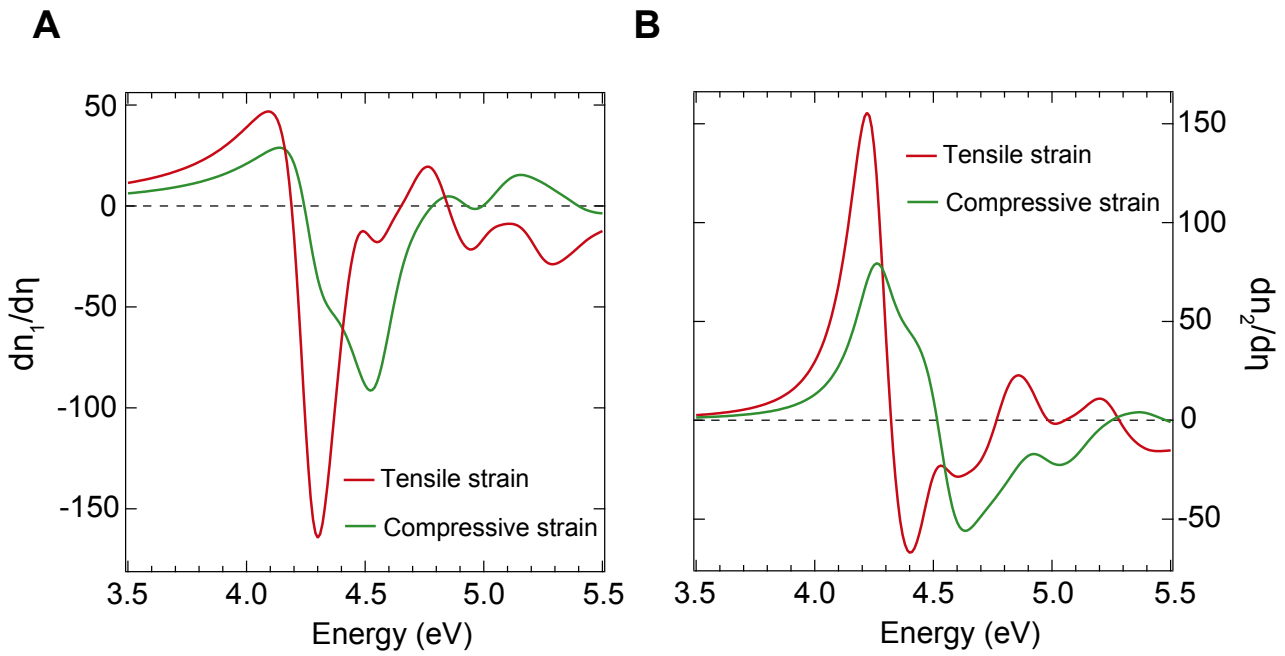

Fig. S4. Calculation of the photoelastic coefficients. Calculated (A) real and (B) imaginary part of the photoelastic coefficient in the presence of a 0.2% tensile (red curves) and compressive (green curves) strain. The red (green) curves have been obtained using the method of the backward (forward) differences.

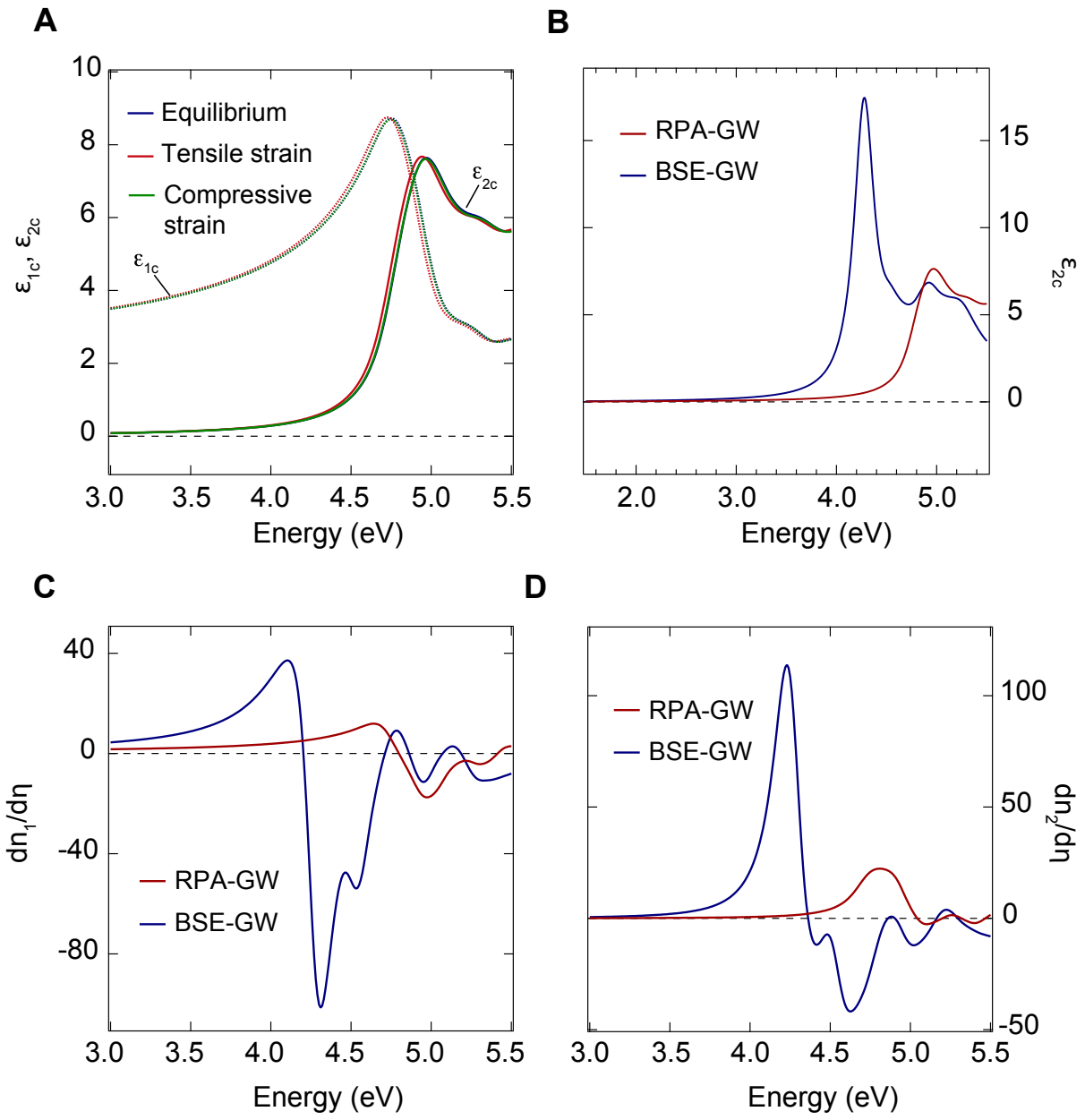

Fig. S5. Comparison between the RPA-GW and BSE-GW results. (A) Calculated real (dashed lines) imaginary (solid lines) parts of the dielectric function in the RPA-GW scheme for the equilibrium (blue curve), strained (red curve) and compressed (green curve) unit cell. (B) Comparison between the imaginary part of the dielectric function calculated in the RPA-GW (red curve) and BSE-GW (blue curve) schemes for the unstrained unit cell. (C) Calculated real part of the photoelastic coefficient in the RPA-GW (red curve) and BSE-GW (blue curve) schemes. (D) Calculated imaginary part of the photoelastic coefficient in the RPA-GW (red curve) and BSE-GW (blue curve) schemes.